Intraseasonal variations in the tropical tropopause temperature revealed by cluster analysis of convective activity

Eriko Nishimoto[1] and Masato Shiotani[1]

[1] Space-time variations of the tropical convective activities and temperatures around the tropical tropopause associated with the intraseasonal oscillation (ISO) are investigated using outgoing longwave radiation (OLR) data from the National Oceanic and Atmospheric Administration and atmospheric fields from the European Centre for Medium-range Weather Forecasts Interim reanalysis data. By performing cluster analysis using the locus of convective activities observed in the unfiltered OLR field, the 72 ISO events selected during the southern summers from 1979–2011 are mainly grouped into four clusters. Two of the clusters exhibit the slow (<2 m/s) propagation speed in the unfiltered OLR field and the others fast (~4 m/s). One cluster characterized as the El Niño phase has the fast speed while passing over the date line and another as the La Niña phase has the slow speed while propagating to ~120°E. Compared with the other two clusters characterized as the weak El Niño-Southern Oscillation phase, the speed is slow while propagating to ~135°E when the SSTs over the Western Pacific are relatively low. Low temperatures around the tropical tropopause appear to the east of the eastward-propagating convection in the tropics and to the west in the subtropics, forming a horseshoe-shaped structure. The strength of the horseshoe-shaped temperature structure is determined by that of the convective activities. Furthermore, the strength and location of the 100 hPa temperature minima differ among the clusters. This study implies that the different ISOs would cause different impacts on the dehydration process depending on their types.

1. Introduction

[2] The tropical tropopause layer (~ 100 hPa; TTL) is a transition layer between the troposphere and the stratosphere and is the primary entrance of tropospheric air passing through to the stratosphere [e.g., *Fueglistaler et al.*, 2009]. Water vapor entering the stratosphere is mainly controlled by the temperatures in this region. *Newell and Gould-Stewart* [1981] presented that the 100 hPa temperatures lower than the zonal average are found over the equatorial Indian Ocean and Western Pacific by using global data from radiosonde network. *Highwood and Hoskins* [1998] analyzed a four year climatology of the 100 hPa temperatures from the European Centre for Medium-Range Weather Forecasts (ECMWF) analyses to show that those low temperatures extend northwestward and southwestward in the subtropics to form a horseshoe-shaped structure.

[3] This horseshoe-shaped temperature structure resembles a stationary wave response known as the Matsuno-Gill pattern [*Matsuno*, 1966; *Gill*, 1980]. This waveform can be described as a combined structure of two types: one represents a Kelvin wave located in the eastern part and the other represents a Rossby wave in the western part. *Highwood and Hoskins* [1998] and *Norton* [2006] demonstrated the Matsuno-Gill response in the tropical tropopause temperature using multiple-layer models. *Hatsushika and Yamazaki* [2003] investigated the transport process through the tropical tropopause in an atmospheric general circulation model and revealed that the cold tropopause temperatures and the circulations in the TTL characterized by the Matsuno-Gill pattern play an important role in the dehydration process.

[4] *Nishimoto and Shiotani* [2012] investigated seasonal and interannual variability of the horseshoe-shaped temperature structure and its association with convective activities using the monthly mean ECMWF 40 year reanalysis (ERA-40) and outgoing longwave radiation (OLR) data. We established the index representing the horseshoe-shaped temperature structure to quantitatively capture its variability. This index revealed the significant relationship with the climatological convective activities around the monsoon regions over the Indian Ocean and Pacific with the seasonal and interannual timescale. During the southern

[1]Research Institute for Sustainable Humanosphere, Kyoto University, Gokasho, Uji, Japan.

Corresponding author: E. Nishimoto, Research Institute for Sustainable Humanosphere, Kyoto University, Gokasho, Uji, Kyoto 611-0011, Japan. (eriko@rish.kyoto-u.ac.jp)
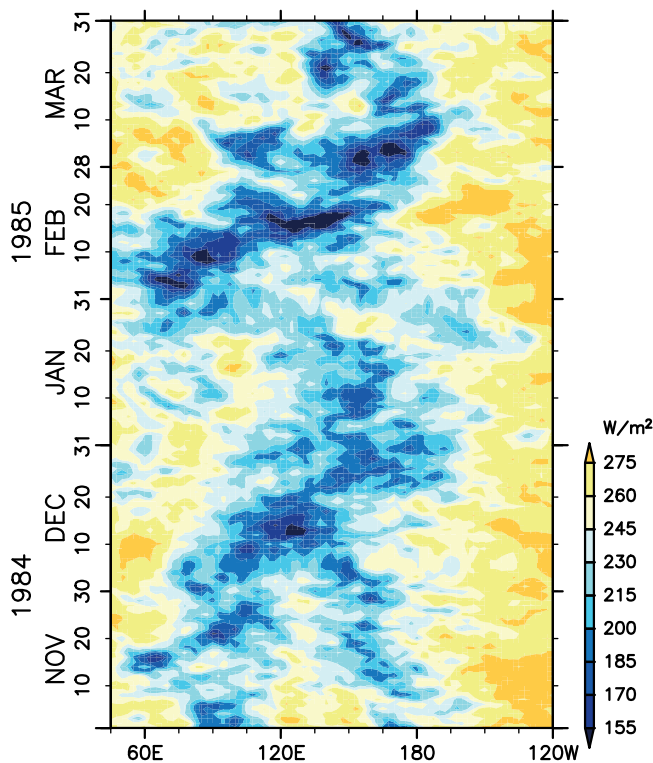
Figure 1. Longitude-time section of the unfiltered outgoing longwave radiation (OLR) (W m^{-2}) averaged over 5°N–15°S for November–March 1984/1985.

summer, the horseshoe-shaped structure index is also related to convective anomalies associated with the El Niño-Southern Oscillation (ENSO) cycle, shifting eastward in El Niño years.

[5] On intraseasonal time scales, the Madden-Julian Oscillation (MJO), an eastward-propagating convective complex with a timescale of 30–60 days, is one of the most dominant disturbances in the tropical atmosphere [e.g., *Madden and Julian*, 1994; *Zhang*, 2005]. Its activities are most vigorous in the southern summer from the Indian Ocean to the Western Pacific in the southern hemisphere [e.g., *Hendon et al.*, 1999; *Zhang*, 2005]. The vertical structure of the MJO extends well into the stratosphere [*Madden and Julian*, 1972; *Kiladis et al.*, 2005] and affects the zonally asymmetric temperature in the tropical tropopause [e.g., *Kiladis et al.*, 2001; *Suzuki and Shiotani*, 2008]. Using the Atmospheric Infrared Sounder (AIRS) data and the Global Positioning System radio occultation (GPS/RO) measurements including the Constellation Observing System for Meteorology, Ionosphere, and Climate (COSMIC) mission, *Tian et al.* [2012] documented the detailed spatiotemporal patterns and vertical structure of the temperature variability in the upper troposphere and lower stratosphere (UT/LS) associated with the MJO. They showed that UT/LS temperature anomalies have structure tilting eastward with height and a Matsuno-Gill-like Kelvin-Rossby wave pattern at 100 hPa, propagating eastward with the deep convection anomaly.

[6] The MJO possibly influences on the dehydration mechanism around the TTL. The UT/LS water vapor anomalies tilt eastward with height similar to the temperature structure and are negative at 100 hPa to the east of the convective anomaly as it propagates into the Western Pacific in composites of MJO events during the southern summer [*Eguchi and Shiotani*, 2004; *Schwartz et al.*, 2008]. *Eguchi and Shiotani* [2004] also observed the 100 hPa cirrus cloud signals to the east of the convective anomaly, attributing the occurrence of the cirrus clouds to the low temperatures produced by the convective system. *Virts and Wallace* [2010] calculated the regression of 80 day high-pass filtered TTL cirrus clouds onto phases of the MJO index derived by *Wheeler and Hendon* [2004]; the MJO index is based on the first two empirical orthogonal function (EOF) modes of OLR and zonal winds at 850 hPa and 200 hPa, and the two modes appear as a quadrature pair that demonstrates a large-scale eastward-propagating intraseasonal signal. In Figure 13 of *Virts and Wallace* [2010], the TTL cirrus cloud signature forms the horseshoe-shaped structure during the phase when the active convection anomaly is centered over the Western Pacific.

[7] Previous studies of the variability in the tropical intraseasonal oscillation (ISO) have emphasized the relationship with El Niño–Southern Oscillation (ENSO). A local response of the MJO to ENSO in the Pacific is mostly observed in the southern summer. *Fink and Speth* [1997] and *Hendon et al.* [1999] showed that MJO activity propagates about 20° longitude farther eastward during El Niño periods than during non-El Niño periods by using the variance of band-pass-filtered OLR; the seasonal mean convective activities also appear further eastward during El Niño periods than during non-El Niño periods [e.g., *Gettelman et al.*, 2001]. A similar result was found by *Gutzler* [1991] by using lower tropospheric zonal wind. *Kessler* [2001] found that the third EOF mode of OLR and zonal wind captures the eastward extension of the MJO envelope during El Niño events.

[8] An example of year-to-year variations of ISO activity unrelated to ENSO has been illustrated by *Hendon et al.* [1999]. In their Figure 1, two ISO events in the southern summer during the weak ENSO periods were displayed; active convections of these events propagate into different longitudes observed in the unfiltered OLR data (similar examples are shown later in Figure 1 in this paper). One type exhibited the character of planetary-scale eastward propagation from the western Indian Ocean to near the date line, and the other, the character of quasi-stationary fluctuations at the longitude of the Australian summer monsoon. The above results imply that seasonal mean convection may affect the longitudinal extent of ISO convective propagation and vice versa. The convective activities of the two ISOs mentioned above also showed different features of the intensity, duration, and propagation speed from each other. Various types of the ISO propagation would have different impacts on the temperatures around the tropical tropopause and consequently the dehydration process in the TTL.

[9] The phase speed of the MJO varies among individual events and during different stages of the life cycle of a given event [e.g., *Hendon and Salby*, 1994; *Izumo et al.*, 2009]. *Roundy* [2012a, 2012b, 2012c] examined the range of propagation speed that is observed in the convective anomaly of

1985-02-09

1985-02-14

1985-02-19

1985-03-01
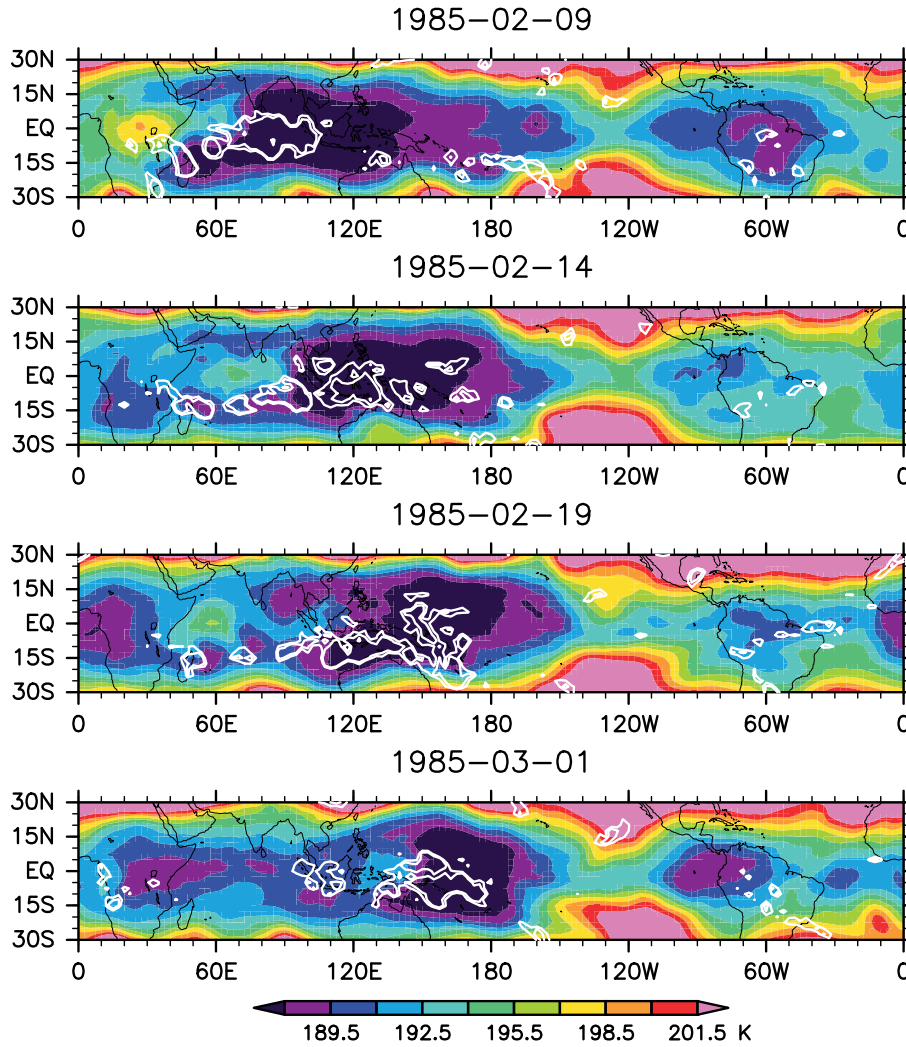
189.5   192.5   195.5   198.5   201.5 K

Figure 2. Longitude-latitude sections of the 100 hPa temperature (K, color) and the unfiltered OLR (W m^{-2}, contour).

the MJO-Kelvin continuum, based on the idea that Kelvin waves and the MJO are not dynamically distinct modes. However, the statistical analysis to distinguish the ISO types according to the propagation speed has not been adequately assessed yet.

[10] In this study, we conduct cluster analysis in order to classify ISO types according to both the phase speed and the longitudinal extent of the eastward propagation. In performing cluster analysis, we employ the unfiltered OLR data by retaining both the ISO and seasonal mean components to investigate interaction between the two. The relationship between the temperatures around the tropical tropopause and the convective activities is then examined. Data sets used in this study are described in section 2. We first present a case study of ISO variations in the convective activity and the 100 hPa temperature during the 1984/1985 southern summer, which was during a weak ENSO period, in section 3. The selection of ISO events and the cluster analysis are then documented in section 4. We investigate the ISO characteristics of the convective activity, horseshoe-shaped temperature structure, 100 hPa temperature, and sea surface temperature (SST) in the clusters in section 5. Finally, section 6 summarizes this paper.

2. Data

[11] Because the main emphasis here is on coherent eastward-propagating convection that occurs predominantly during the southern summer [e.g., *Hendon et al.*, 1999; *Zhang*, 2005], this study is restricted to the southern summer season. Daily OLR data obtained from the National Oceanic and Atmospheric Administration (NOAA) satellites are available with a 2.5° grid spatial resolution [*Gruber and*
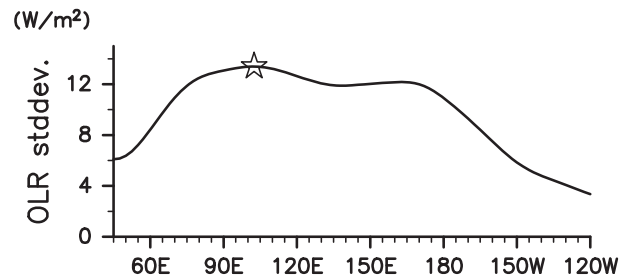
Figure 3. Standard deviation at each longitude of the band-pass-filtered OLR data averaged over 5°N–15°S. The open star indicates the location of maximum standard deviation.
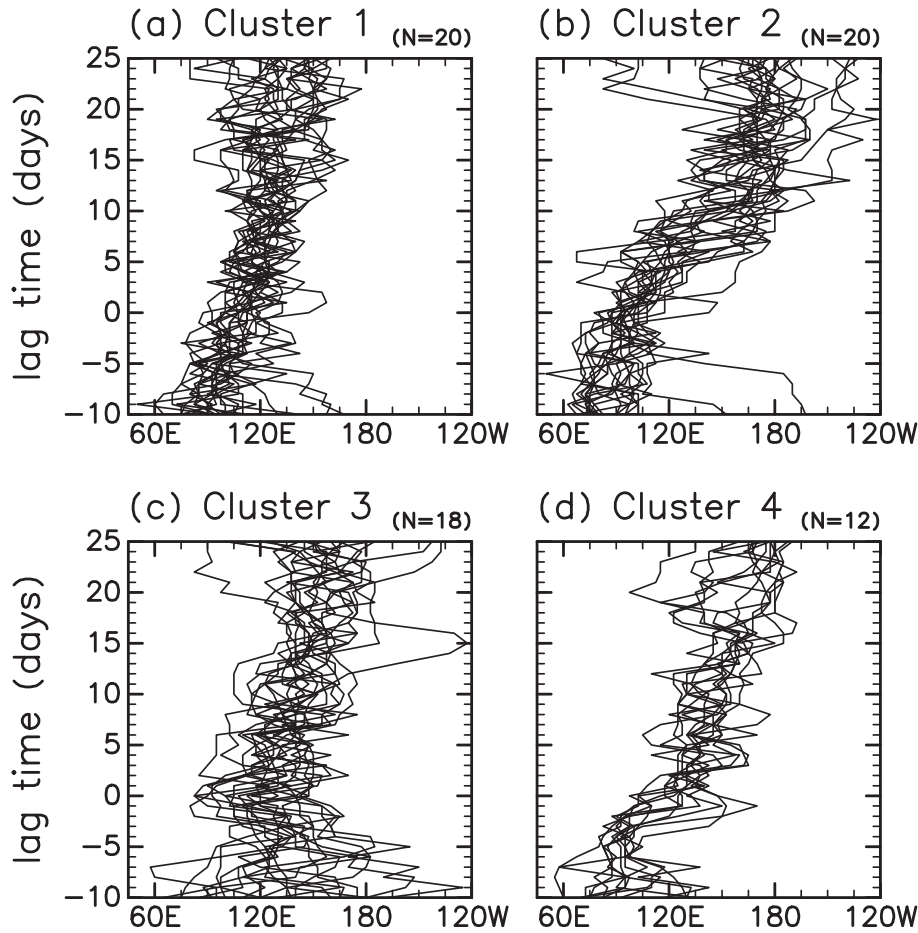
Figure 4. Longitude-time sections of the ISO locus for every event included in (a) Cluster 1, (b) Cluster 2, (c) Cluster 3, and (d) Cluster 4.

Krueger, 1984]. We used 32 complete southern summer seasons from January 1979 to December 2011. The OLR data are averaged between 5°N and 15°S, where the convective component of the ISO is most active in the southern summer [e.g., *Hendon et al.*, 1999].

[12] Other meteorological variables such as temperature, wind, and SST come from the European Centre for Medium-range Weather Forecasts (ECMWF) global reanalysis ERA-Interim data [*Dee et al.* 2011]. The original data are provided at 6 h intervals with a 1.5° grid spatial resolution, but in this study we reconstruct them with the same time, and spatial resolutions as those used in the OLR data, that is, a daily mean with a 2.5° grid spatial resolution. We use the 100 hPa temperature data to investigate variations in the temperature around the tropical tropopause. The temperatures at the 100 hPa level, which is generally located lower than the cold-point and lapse-rate tropopause during the southern summer, are a few degrees higher than the cold-point and lapse-rate tropopause temperatures [*Seidel et al.*, 2001].

3. Case Study of the 1984/1985 Southern Summer

[13] Figure 1 illustrates a longitude-time section of the daily (unfiltered) OLR averaged between 5°N and 15°S

for November–March 1984/1985. This year is at the weak ENSO period. We detect two ISO events propagating from the Indian Ocean to the Pacific during this period (the method of selecting ISO events will be described in section 4.1): the first one during the middle of November through December, and the second one during February through the beginning of March. These two events have different propagation features in the unfiltered OLR field; the second one propagates much faster and farther than the first one while having the stronger active convection of longer duration than the first one. We will perform cluster analysis according to the ISO propagation features of the active convection observed in the unfiltered OLR field in the next section. The above two events will be grouped into Clusters 3 and 4, respectively.

[14] Figure 2 shows the 100 hPa temperature variations associated with the eastward-propagating convection of the second ISO event (February through the beginning of March in 1985). The active convection propagates from the Indian Ocean to near the date line, and accompanies low temperatures to the east around the equator and to the west around 10°N and 10°S. These low temperatures form the horseshoe-shaped structure, which resembles a super position of the Rossby and Kelvin responses and is known as the Matsuno-
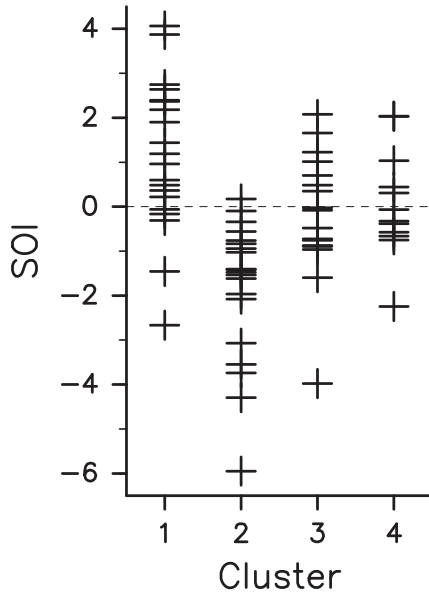
Figure 5. Southern Oscillation Index (SOI) values for the ISO events in each cluster. The SOI values are from a 5 month running mean.

Gill pattern. Similar low temperatures were observed by *Eguchi and Shiotani* [2004] who created composites of the 100 hPa temperature relative to the passage of five different MJO-related convective systems.

[15] We find that low temperatures exist over both equatorial South America and Africa in Figure 2. The low temperatures appear over South America on 9 February and 1 March and over Africa on 19 February and 1 March, and are more narrowly confined to the equatorial belt than those over the Western Pacific. The convective activities around the low temperatures exhibit no significant difference during this period. These results are in agreement with the previous study of *Hendon and Salby* [1994], which indicated that the upper-level perturbation associated with the MJO circumnavigates the equatorial belt. Because the low temperatures over both equatorial South America and Africa do not form the horseshoe-shaped structure and are not directly connected to the variability in the convective activities, we will not discuss them further in this paper.

4. Cluster Analysis of ISO Events

4.1. Selection of ISO Events

[16] The ISO signal is isolated as in *Suzuki and Shiotani* [2008], by space-time filtering OLR to retain only eastward-propagating signals of wavenumbers 1–10 with periods between 23 and 90 days. Figure 3 shows the standard deviation of the ISO signal averaged between 5°N and 15°S during the southern summer (November–March). As noted in many previous studies [e.g., *Zhang*, 2005], the convective component of the ISO is most active over the high mean SST warm pool regions of the Indian Ocean around 90°E and the Western Pacific around 165°E. The convective

component is generally much weaker over the Maritime Continent around 135°E than over the surrounding oceans. We use the longitude having the maximum standard deviation (σ_{max} = 13.382 W/m^2), 102.5°E, as a reference point.

[17] The time series of the ISO signal averaged over 5°N–15°S at the reference point is used as an index of the ISO. Using a convention similar to those of *Kiladis et al.* [2002] and *Eguchi and Shiotani* [2004], the day having the lowest ISO index value less than $-1\sigma_{max}$ (-13.382 W/m^2) is referred as day 0 (the key day). The key days are searched between November and March and a total of 72 ISO events are selected on the basis of this index in the 32 southern summers. Every event has different features, such as a different propagation speed and intensity in the observed unfiltered OLR field. Cluster analysis will then be performed according to these features in the next subsection.

4.2. Cluster Analysis

[18] To categorize the ISO events according to the propagation feature observed in the unfiltered OLR field, we conduct cluster analysis by using the ISO locus, which is selected in the following way. We first search for the unfiltered OLR minimum point around the reference point (102.5°E ± 45.0°E) at the key day. After the key day the OLR minimum point is selected between the ±45° longitude range around the minimum point of the prior day, and before the key day around the minimum point of the following day. We used the ISO locus between day –5 and day 20, because the OLR values are on average low (under 200 W/m^2) during this period.

[19] We perform cluster analysis with Ward's method [*Wilks*, 2011], which is one of the hierarchical clustering methods and defined based on the notion of square error. In Ward's method, at each clustering step, the value of the sum-of-square error is computed for every possible merger of two clusters. The merger, which produces the smallest increase in the value of sum-of-square error, is taken to be the clustering of this step. This process is repeated in each step until the growth rate of the sum-of-square error suddenly becomes large. Initially, each cluster contains only one object; hence, the value of the sum-of-square error at the beginning is zero.

[20] After the cluster analysis, the total number of 72 ISO events are grouped into five clusters, which contain 20, 20, 18, 12, and 2 events, respectively. No distinct seasonal bias appears in each cluster (not shown). Figure 4 displays the ISO locus for the top four clusters (Clusters 1–4). We find two major categories for the ISO propagation speed, as observed in the unfiltered OLR field. The speeds are estimated by applying a linear least squares fit to the OLR minima points observed in the composite unfiltered OLR field (Figure 6), and the correlation coefficients are more than 0.8. The speed of one category is estimated to be about 2.0 m/s (Figures 4a and 4c for Clusters 1 and 3, respectively) and that of the other is about twice as fast for it to be about 4.5 m/s and 3.4 m/s (Figures 4b and 4d for Clusters 2 and 4, respectively). As shown in Figure 5, most of the events in Clusters 1 and 2 occurred in the La Niña and El Niño periods, respectively, while most of the events in Clusters 3 and 4 occurred in the weak ENSO periods. SST variations over
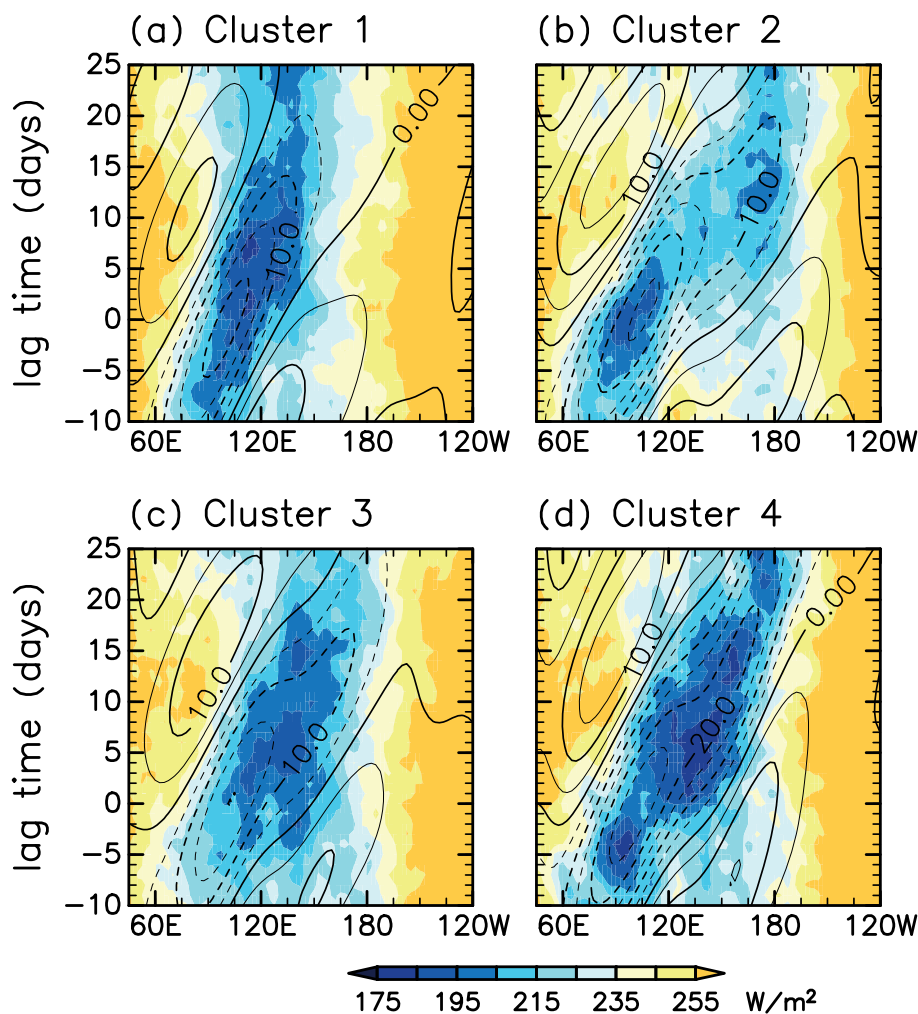
Figure 6. Longitude-time sections of the composite unfiltered OLR (W m^{-2}, color) and band-pass-filtered OLR (W m^{-2}, contours) averaged over 5°N–15 °S. Contour intervals are 5 W m^{-2}.

the Pacific would cause the differences in the propagation characteristics, as will be seen in Figure 11 and discussed in section 5.4.

[21] The ISO signals detected in the unfiltered OLR field for Clusters 1 and 3 propagate eastward until about 120°E and 135°E, respectively, with relatively slow propagation speeds (Figures 4a and 4c, respectively). Clusters 2 and 4 (Figures 4b and 4d, respectively) exhibit a faster propagation speed equivalent to the ISO phase speed, which is derived from the anomalous OLR field [e.g., *Hendon and Salby*, 1994]. We find that each ISO event contains high-frequency variability in the unfiltered OLR field such as eastward-propagating disturbances at the speed of a convectively coupled Kelvin wave and westward-moving disturbances with periods of 2 and 5 days [*Nakazawa*, 1988; *Zhang*, 2005]. Cluster 5 consists of two events in the strong El Niño years and exhibits quasi-stationary fluctuations over the Indian Ocean with weak convective activities (not shown); therefore, the following analyses are focused on the top four clusters.

5. Characteristics of Each ISO Cluster

5.1. Convective Activity

[22] Figure 6 shows longitude-time sections of the composite band-pass-filtered and unfiltered OLR values averaged between 5°N and 15°S for Clusters 1–4. We find that the propagation speeds of the convective activities observed in the unfiltered OLR field are much slower in Clusters 1 and 3 compared with those in Clusters 2 and 4, as shown in Figure 4. The speed observed in the band-pass-filtered OLR fields are nearly identical among the four clusters.

[23] The quasi-stationary convective area observed in the unfiltered OLR field (colors in Figure 6) appears around 135°E in Cluster 3 and to the west of that in Cluster 1 around 120°E as the active convective area in La Niña years occurs over the Indian Ocean and Western Pacific in the little farther west of that in normal years [e.g., *Gettelman et al.*, 2001]. Peaks of the convective activities observed in the unfiltered OLR field occur at day 7 in Cluster 1 and
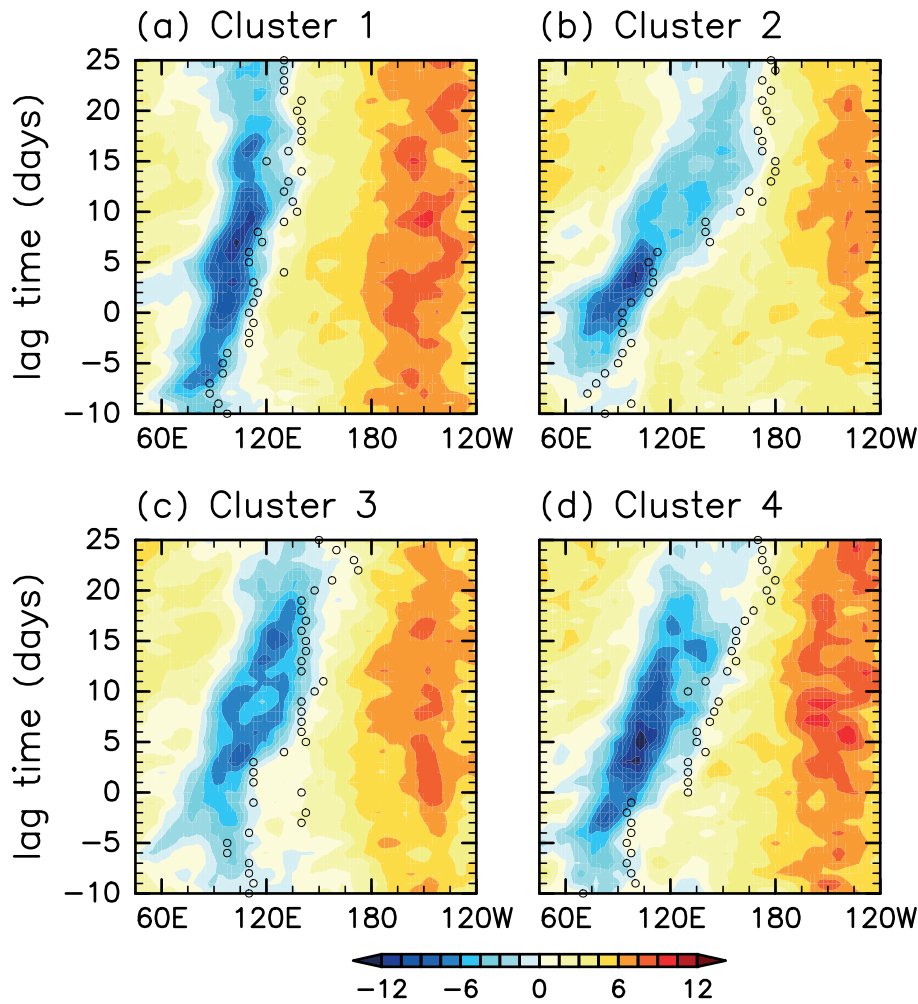
Figure 7. Same as Figure 6, but for HSI-1. Open circles show location of the minimum of the unfiltered OLR averaged over 5°N–15°S at each day.

at day 6 in Cluster 3, when the ISO signals observed in the band-pass-filtered field (contours) pass over the quasi-stationary areas.

[24] We find in the unfiltered OLR field (colors in Figure 6) that the eastward-propagating convective activities in Cluster 2 penetrate farther eastward into the central Pacific than those in Cluster 4. This difference in the propagation features is also detected in the band-pass-filtered OLR field (contours in Figure 6) in agreement with the previous ISO studies in the El Niño southern summers [e.g., *Fink and Speth*, 1997; *Hendon et al.*, 1999]. The convective activities observed in the unfiltered OLR fields for Clusters 2 and 4 each have two peaks in the Indian and Pacific Oceans, respectively. The peaks in Cluster 4 appear around 90°E at day –5 and around 150°E at day 5, while those in Cluster 2 appear around 90°E at day 0 and around 180°E at day 13 with weaker activities than those in Cluster 4.

5.2. The Horseshoe-Shaped Temperature Structure

[25] As seen in Figure 2, the low temperatures, which form the horseshoe-shaped structure, propagate eastward and are accompanied with the eastward-moving active convection. We derive the horseshoe-shaped structure index
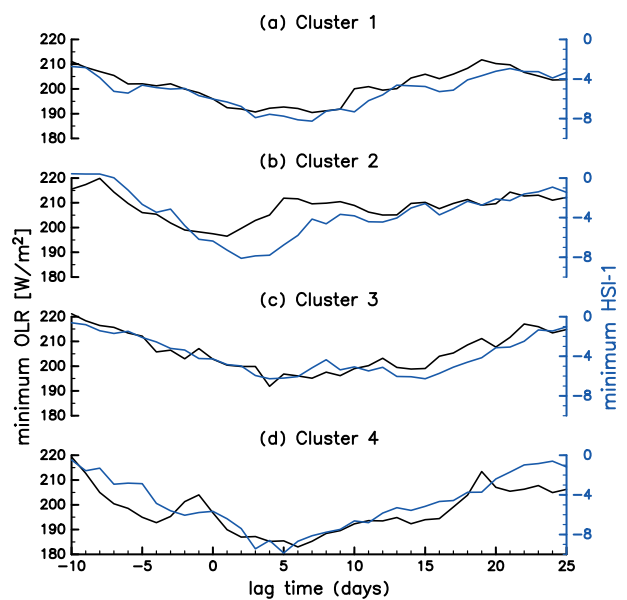

Figure 8. Minima of the composite unfiltered OLR (W m^{-2}, black line) and HSI-1 (blue line) time series.
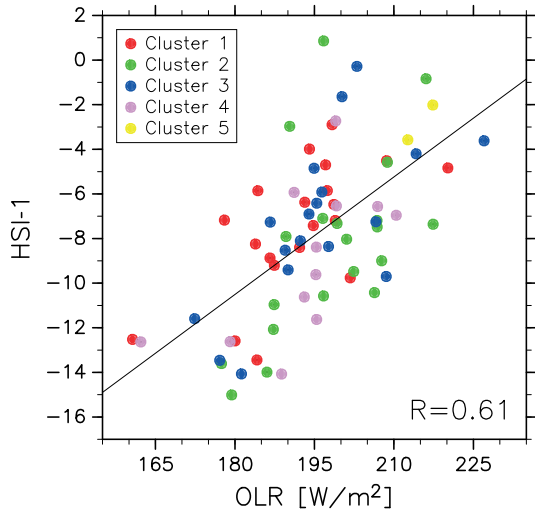
Figure 9. Scatterplots of the unfiltered OLR and HSI-1 values averaged between day –2 and day 2. Red, green, blue, pink, and yellow circles represent Clusters 1–5, respectively. (HSI-1) by using the daily mean temperature data at 100

hPa as in *Nishimoto and Shiotani* [2012]. Because this structure resembles the Matsuno-Gill pattern, the two preliminary indices, HSI-R and HSI-K, are defined to represent the Rossby and Kelvin responses, respectively. The index HSI-R, which is a function of longitude and time, is calculated by a curvature of the 100 hPa temperature along the meridional circle at the equator. When low temperatures occur in the subtropics as the Rossby response, this index becomes negative. The index HSI-K, which is also a function of longitude and time, is calculated by a zonal gradient of the 100 hPa temperature along the equator. When the temperature structure represents the Kelvin response, this index becomes negative. In the horseshoe-shaped structure, negative HSI-K values are located slightly to the east of the negative HSI-R values, which is in agreement with the Matsuno-Gill pattern.

[26] The HSI-R and HSI-K values may change accordingly with a positive correlation in response to heating generated by convective activities. Because of this, the index HSI-1 is derived by results of EOF analysis applied to HSI-R and HSI-K values and projects a positive linear relationship between them as a function of longitude x and time t: HSI-1$(x, t) = 1.65 \times$ HSI-R$(x, t) + 1.90 \times$ HSI-K$(x+12.5°, t)$.
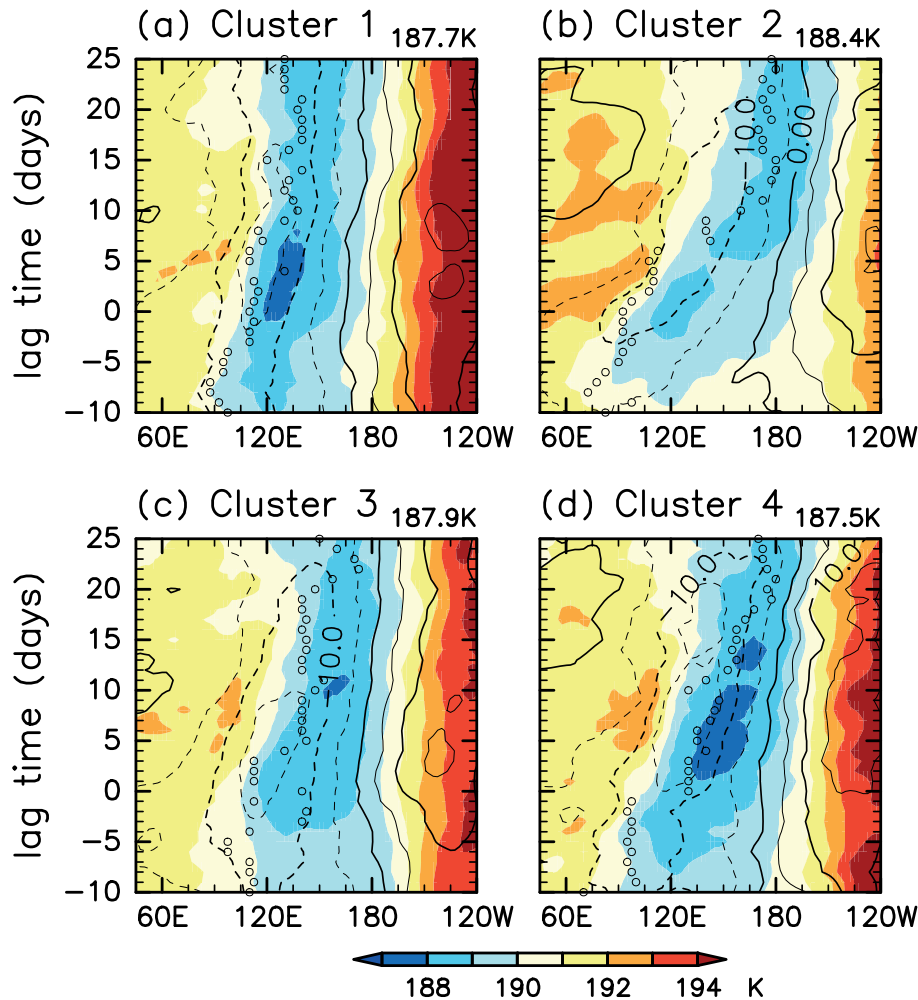

Figure 10. Same as Figure 6, but for the temperature (K, color) and zonal wind (m s^{-1}, contour) at 100 hPa averaged over 15°N–15°S. Contour intervals are 5 m s^{-1}. Temperature minima are shown above each panel.
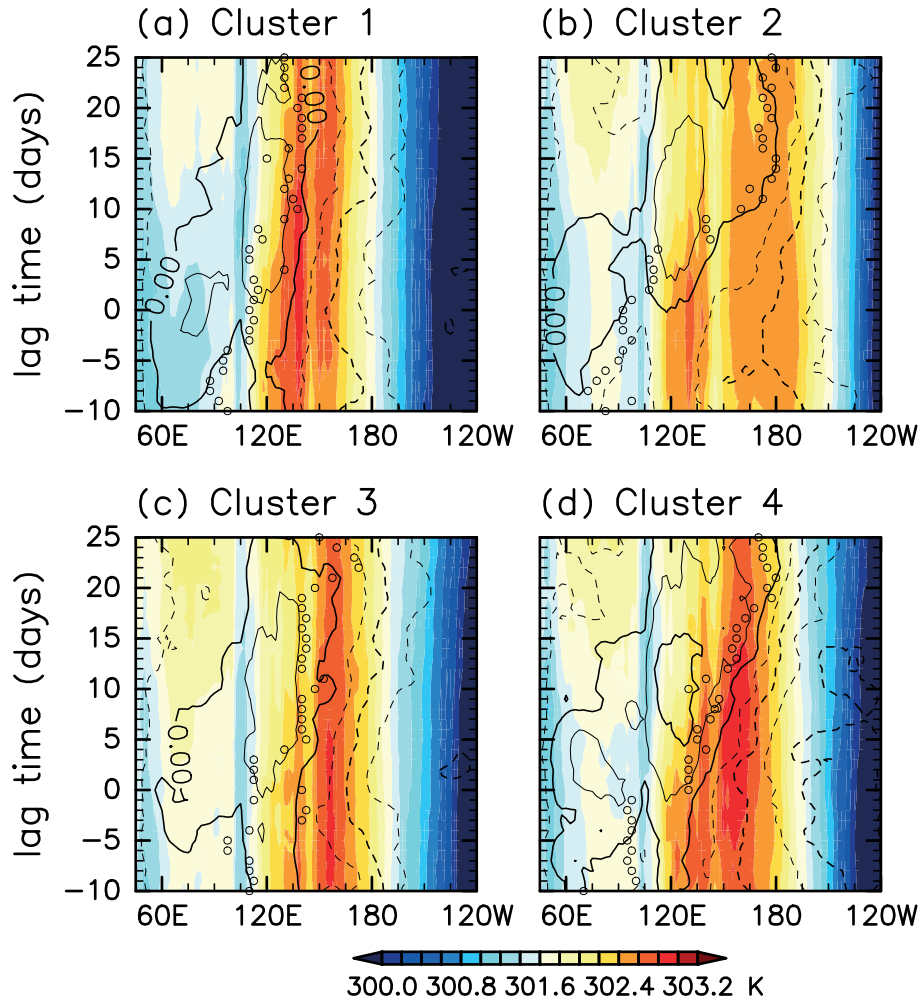
Figure 11. Same as Figure 6, but for the SST (K, color) and zonal wind at 10 m (m s^{-1}, contour) averaged over 5°N–15°S. Contour intervals are 1.5 m s^{-1}.

When the HSI-1 value is negative, the temperature field should be representative of the horseshoe-shaped structure. Since we set the longitude of HSI-R as a base longitude with the longitude phase lag of HSI-K, the negative HSI-1 values appear over the western part of the horseshoe-shaped structure. The HSI-1 value is expected to change accordingly in response to heating generated by the convective activities associated with the ISO.

[27] As presented in Figure 7, the propagation and intensity features observed in the HSI-1 fields display similarities to those observed in the unfiltered OLR fields. The negative HSI-1 peaks occur about 10°–20° west of the convection centers (open circles). This longitudinal-phase relationship is similar to that observed in the climatological response adjacent to monsoon areas [*Nishimoto and Shiotani*, 2012]. Negative HSI-1 values propagate relatively slowly in Clusters 1 and 3. The peak occurs with strong negative values around 105°E in Cluster 1 and with relatively weak negative values around 120°E in Cluster 3. In contrast, Clusters 2 and 4 exhibit fast-propagating features in the HSI-1 fields. Cluster 4 has strong negative HSI-1 peaks around 90°E and 105°E. A significant peak in Cluster 2 occurs only around 105°E while the unfiltered OLR field has two peaks (Figure 6b). However, the correlation coeffi-

cient between the HSI-1 and unfiltered OLR values shows significant values for each cluster.

[28] Figure 8 shows time series of the composite unfiltered OLR and HSI-1 values between day –10 and day 25 for Clusters 1–4, which are averaged over ±15° of longitude around the minimum locations. The maximum correlation coefficient is 0.92 at a 1 day lag (OLR values preceding HSI-1 values) in Cluster 1, 0.87 at a 2 day lag in Cluster 2, 0.92 at a 1 day lag in Cluster 3, and 0.88 at a 1 day lag in Cluster 4. The 5% significance level is 0.34 when the number of degrees of freedom (N) is 34.

[29] Event-to-event variations in the intensity of convective activities and horseshoe-shaped temperature structure are also related to each other. Figure 9 shows a scatterplot of the OLR and HSI-1 values, which are averaged over ±15° of longitude around the minimum locations and between day –2 and day 2 in each event. Significant correlations are found both for all events ($r = 0.61$ and N= 72) and for events in each cluster ($r = 0.64$ and $N = 20$ in Cluster 1, $r = 0.56$ and $N = 20$ in Cluster 2, $r = 0.67$ and $N = 18$ in Cluster 3, and $r = 0.62$ and $N = 12$ in Cluster 4). The 5% significance levels are 0.30 at $N = 72$, 0.44 at $N = 20$, 0.47 at $N = 18$, and 0.58 at $N = 12$. The significant relationships, both in the ISO life cycle and in

the event-to-event variation, indicate that the heating generated by the convective activities associated with the ISO could induce the horseshoe-shaped pattern and these could propagate eastward together.

5.3. The 100 hPa Temperature

[30] Figure 10 shows the composite temperature and zonal wind fields at the 100 hPa level averaged over 15°N–15°S for Clusters 1–4. Low temperatures appear about 30° eastward of the centers of active convection in each cluster, and the easterly wind is located almost over the convection center. Similar relationships have been observed in anomaly fields from the UT/LS in previous studies of the ISO [e.g., *Hendon and Salby*, 1994; *Eguchi and Shiotani*, 2004]; temperature anomalies and zonal wind anomalies are observed to be almost in quadrature, which can be regarded as the Kelvin wave response to convective heating.

[31] The 100 hPa temperature minima in the ISO life cycle are significantly correlated with the HSI-1 minima. The correlation coefficient is 0.71 in Cluster 1, 0.50 in Cluster 2, 0.91 in Cluster 3, and 0.83 in Cluster 4. Although the relationship in the event-to-event variation is not large ($r = 0.38$), the low temperatures around the tropical tropopause vary accordingly with the horseshoe-shaped structure at least during the ISO life cycle. As *Hatsushika and Yamazaki* [2003] presented, the horseshoe-shaped temperature structure would effectively dehydrate air in the TTL together with the accompanying circulations. We also find that the minimum temperature differs among the clusters. The minimum is 187.7 K at day 4 and 132.5°E in Cluster 1, 188.4 K at day 12 and 180.0°E in Cluster 2, 187.9 K at day 11 and 162.5°E in Cluster 3, and 187.5 K at day 9 and 155.0°E in Cluster 4. *Eguchi and Shiotani* [2004] attributed the occurrence of the cirrus clouds to the low temperatures in the TTL associated with the ISO. These results imply that the dehydration and troposphere-stratosphere exchange processes associated with the ISO would occur at different locations and that the contributions to those processes would be different in the clusters.

5.4. Sea Surface Temperature

[32] Figure 11 shows the composite SST and zonal wind fields at 10 m averaged over 5°N–15°S for Clusters 1–4. The MJO may induce intraseasonal perturbations in SST by disturbing surface fluxes of heat, momentum, and freshwater [e.g., *Zhang*, 1996; *Jones et al.*, 1998; *Zhang and McPhaden*, 2000]. We find that every cluster has the convective centers (open circles) in between the surface westerly and easterly, and the westerlies are stronger than the easterlies. This situation is similar to that observed in anomalies of SST and surface wind associated with the MJO structure in the equatorial Indian Ocean and Western Pacific [*Hendon and Salby*, 1994].

[33] The average SST distributions in Clusters 1 and 2 display the characteristics of those observed during the La Niña and El Niño periods, respectively, and the distributions in Clusters 3 and 4 display the characteristics of those observed during weak ENSO [e.g., *Gettelman et al.*, 2001]. High SSTs in Cluster 1 are confirmed over the Western Pacific around 135°E, and low SSTs extend from around the date line to the east. High SSTs in Cluster 2 are broadly distributed between 120°E and 190°E, and low

SSTs extend from 240°E to the east. The SSTs in Clusters 3 and 4 are high over 120°E–180°E and are low from 210°E to the east.

[34] The eastward propagation speed of the convective centers in Cluster 4 is faster than that in Cluster 3, as already discussed in sections 4.2 and 5.1. Although the average SST distributions are observed to be nearly identical between Clusters 3 and 4, the SSTs in Cluster 4 are high around 120°E compared to those in Cluster 3. This implies that during the weak ENSO periods the SSTs over the Western Pacific would affect the eastward propagation speed of the convective activity associated with the ISO. High SST occurs east of the date line in Cluster 2, and the convective centers propagate over the date line. The farther eastward propagation of the MJO envelope during the El Niño periods is a well-known feature that is observed in the band-pass-filtered data [e.g., *Fink and Speth*, 1997; *Hendon et al.*, 1999; *Kessler*, 2001].

6. Summary

[35] We have investigated space-time variations of the tropical convective activity and temperature around the tropical tropopause associated with the ISO, such as the MJO, by using NOAA/OLR and ERA-Interim data. In the case study of the 1984/1985 southern summer, which is during the weak (normal) ENSO period, we showed that various types of the convective propagation features associated with the ISO are observed in the unfiltered OLR field. These convective activities accompany low temperatures to their east in the tropics and to their west in the subtropics around the tropical tropopause. These low temperatures form a horseshoe-shaped structure, which resembles the Matsuno-Gill pattern.

[36] The 72 ISO events that occur during the southern summer from January 1979 to December 2011 were first selected with respect to the time series at the reference point (102.5°E) where variations of the band-pass-filtered OLR averaged over 5°N–15°S are largest. We then performed cluster analysis with Ward's method by using the locus of the unfiltered OLR minima in the ISO events, and categorized the propagation features into five clusters, which consist of 20, 20, 18, 12, and 2 events.

[37] Most of the events in Clusters 1 and 2 occur during the La Niña and El Niño periods, respectively, and those in Clusters 3 and 4 during the weak ENSO periods. In association with the ISO, the convective activities observed in the unfiltered OLR field in Clusters 1 and 3 have a relatively slow speed (<2 m/s) and propagate to 120°E and 135°E, respectively. The faster (~ 4 m/s) convective activities in Clusters 2 and 4 propagate into the central Pacific. The composite SST field reveals the following facts about the convective propagation. During the weak ENSO periods (Clusters 3 and 4), the propagation speed is slow when the SSTs over the Western Pacific are relatively low. During the El Niño periods (Cluster 2), as the eastern edge of the warm pool extends over the date line, so does the active convection.

[38] To investigate space-time variability in the horseshoe-shaped temperature structure associated with the ISO, we used the horseshoe-shaped structure index (HSI-1), which was defined in *Nishimoto and Shiotani* [2012]. The

composite HSI-1 fields have similar features to those of OLR, located about 10°–20° west of the active convective area. Both the ISO life cycle and event-to-event variation in the HSI-1 values are significantly correlated with those in the unfiltered OLR values. Those results imply that the convective heating associated with the ISO induces the horseshoe-shaped temperature structure around the tropical tropopause.

[39] Low temperatures at 100 hPa change accordingly with the HSI-1 minima at least in the ISO life cycle. Furthermore, the strength and location of the temperature minima at 100 hPa are different among the ISO clusters. We could suggest from these results that the different types of the ISO would be different impacts on the troposphere-stratosphere exchange such as the dehydration process depending on their types, considering the previous studies, which investigated the possible influence of the the ISO and horseshoe-shaped structure on the troposphere-stratosphere exchange process in the TTL; *Eguchi and Shiotani* [2004] and *Virts and Wallace* [2010] showed that the strong signal of the cirrus clouds appears accompanied with the ISO active convection. *Hatsushika and Yamazaki* [2003] demonstrated that the enhanced upward motion penetrating into the TTL occurs over the active convection region and the circulation characterized by the Matsuno-Gill pattern entrains the tropospheric air parcels. These air parcels then pass over the cold tropopause region several times during the slow ascent in the TTL.

[40] Diagnostic interpretation of reanalysis data [*Kerr–Munslow and Norton*, 2006; *Randel et al.*, 2008] and model simulations [*Boehm and Lee*, 2003; *Norton*, 2006; *Garny et al.*, 2011] revealed that much of the upwelling in the TTL is forced by the dissipation of tropical waves such as the Rossby waves. In Figure 6 of *Eguchi and Shiotani* [2004], the slow ascent is detected over the cold tropopause region in association with the ISO using the ECMWF operational data. Therefore, the upwelling in the TTL may occur over the horseshoe-shaped temperature structure associated with the ISO.

[41] This study clearly revealed the intraseasonal variability in the convective activities and temperatures around the tropical tropopause during the southern summer by employing cluster analysis according to the propagation features of the convective centers. A better understanding of lower troposphere conditions that would induce variations in the propagation features of the convective activities is needed.

References

Boehm, M. T., and S. Lee (2003), The implications of tropical Rossby waves for tropical tropopause cirrus formation and for the equatorial upwelling of the Brewer-Dobson circulation, *J. Atmos. Sci.*, *60*(2), 247–261, doi:10.1175/1520-0469(2003)060<0247:TIOTRW>2.0.CO;2.

Dee, D. P., et al. (2011), The ERA-Interim reanalysis: Configuration and performance of the data assimilation system, *Quart. J. R. Meteorol. Soc.*, *137*(656), 553–597, doi:10.1002/qj.828.

Eguchi, N., and M. Shiotani (2004), Intraseasonal variations of water vapor and cirrus clouds in the tropical upper troposphere, *J. Geophys. Res.*, *109*(D12), 1–11, doi:10.1029/2003JD004314.

Fink, A., and P. Speth (1997), Some potential forcing mechanisms of the year-to-year variability of the tropical convection and its intraseasonal (25–70 day) variability, *Int. J. Climatol.*, *17*(14), 1513–1534, doi:10.1002/(SICI)1097-0088(19971130)17:14<1513::AID-JOC210>3.0.CO;2-U.

Fueglistaler, S., A. E. Dessler, T. J. Dunkerton, I. Folkins, Q. Fu, and P. W. Mote (2009), Tropical tropopause layer, *Rev. Geophys.*, *47*(1), RG1004, doi:10.1029/2008RG000267.

Garny, H., M. Dameris, W. Randel, G. E. Bodeker, and R. Deckert (2011), Dynamically forced increase of tropical upwelling in the lower stratosphere, *J. Atmos. Sci.*, *68*(6), 1214–1233, doi:10.1175/2011JAS3701.1.

Gettelman, A., W. J. Randel, S. Massie, F. Wu, W. G. Read, and J. M. Russell (2001), El Niño as a natural experiment for studying the tropical tropopause region, *J. Climate*, *14*(16), 3375–3392.

Gill, A. E. (1980), Some simple solutions for heat-induced tropical circulation, *Quart. J. R. Meteorol. Soc.*, *106*(449), 447–462, doi:10.1002/qj.49710464905.

Gruber, A., and A. F. Krueger (1984), The status of the NOAA outgoing longwave radiation data set, *Bull. Am. Meteorol. Soc.*, *65*(9), 958–962.

Gutzler, D. (1991), Interannual fluctuations of intraseasonal variance of near-equatorial zonal winds, *J. Geophys. Res.*, *96*, 3173–3185.

Hatsushika, H., and K. Yamazaki (2003), Stratospheric drain over Indonesia and dehydration within the tropical tropopause layer diagnosed by air parcel trajectories, *J. Geophys. Res.*, *108*, 4610, doi:10.1029/2002JD002986.

Hendon, H. H., and M. L. Salby (1994), The life cycle of the Madden-Julian oscillation, *J. Atmos. Sci.*, *51*(15), 2225–2237, doi:10.1175/1520-0469(1994)051<2225:TLCOTM>2.0.CO;2.

Hendon, H. H., C. Zhang, and J. D. Glick (1999), Interannual variation of the Madden-Julian oscillation during austral summer, *J. Climate*, *12*(8), 2538–2550, doi:10.1175/1520-0442(1999)012<2538:IVOTMJ>2.0.CO;2.

Highwood, E. J., and B. J. Hoskins (1998), The tropical tropopause, *Quart. J. R. Meteorol. Soc.*, *124*(549), 1579–1604, doi:10.1002/qj.49712454911.

Izumo, T., S. Masson, J. Vialard, C. Boyer Montegut, S. K. Behera, G. Madec, K. Takahashi, and T. Yamagata (2009), Low and high frequency Madden-Julian oscillations in austral summer: Interannual variations, *Clim. Dyn.*, *35*(4), 669–683, doi:10.1007/s00382-009-0655-z.

Jones, C., D. E. Waliser, and C. Gautier (1998), The influence of the Madden-Julian oscillation on ocean surface heat fluxes and sea surface temperature, *J. Climate*, *11*(5), 1057–1072, doi:10.1175/1520-0442(1998)011<1057:TIOTMJ>2.0.CO;2.

Kerr-Munslow, A. M., and W. A. Norton (2006), Tropical wave driving of the annual cycle in tropical tropopause temperatures. Part I: ECMWF analyses, *J. Atmos. Sci.*, *63*(5), 1410–1419, doi:10.1175/JAS3697.1.

Kessler, W. S. (2001), EOF representations of the Madden-Julian oscillation and its connection with ENSO, *J. Climate*, *14*(13), 3055–3061, doi:10.1175/1520-0442(2001)014<3055:EROTMJ>2.0.CO;2.

Kiladis, G. N., K. H. Straub, G. C. Reid, and K. S. Gage (2001), Aspects of interannual and intraseasonal variability of the tropopause and lower stratosphere, *Quart. J. R. Meteorol. Soc.*, *127*(576), 1961–1983, doi:10.1002/qj.49712757606.

Kiladis, G. N., D. J. Seidel, and K. H. Straub (2002), Variability of the tropical tropopause, *SPARC Newsletter*, *18*, 18–22.

Kiladis, G. N., K. H. Straub, and P. T. Haertel (2005), Zonal and vertical structure of the Madden-Julian oscillation, *J. Atmos. Sci.*, *62*(8), 2790–2809, doi:10.1175/JAS3520.1.

Madden, R. A., and P. R. Julian (1972), Description of global-scale circulation cells in the tropics with a 40–50 day period, *J. Atmos. Sci.*, *29*(6), 1109–1123, doi:10.1175/1520-0469(1972)029<1109:DOGSCC>2.0.CO;2.

Madden, R. A., and P. R. Julian (1994), Observations of the 40–50-day tropical oscillation—A review, *Mon. Weather Rev.*, *122*(5), 814–837.

Matsuno, T. (1966), Quasi-geostrophic motions in the equatorial area, *J. Meteorol. Soc. Japan*, *44*(1), 25–43.

Nakazawa, T. (1988), Tropical super clusters within intraseasonal variations over the western pacific, *J. Meteorol. Soc. Japan*, *66*(6), 823–839.

Newell, R. E., and S. Gould-Stewart (1981), A stratospheric fountain? *J. Atmos. Sci.*, *38*(12), 2789–2796.

Nishimoto, E., and M. Shiotani (2012), Seasonal and interannual variability in the temperature structure around the tropical tropopause and its relationship with convective activities, *J. Geophys. Res.*, *117*(D2), D02,104, doi:10.1029/2011JD016936.

Norton, W. A. (2006), Tropical wave driving of the annual cycle in tropical tropopause temperatures. Part II: Model results, *J. Atmos. Sci.*, *63*(5), 1420–1431, doi:10.1175/JAS3698.1.

Randel, W. J., R. Garcia, and F. Wu (2008), Dynamical balances and tropical stratospheric upwelling, *J. Atmos. Sci.*, *65* (11), 3584–3595, doi:10.1175/2008JAS2756.1.

Roundy, P. E. (2012a), Tracking and prediction of large-scale organized tropical convection by spectrally focused two-step space-time EOF analysis, *Quart. J. R. Meteorol. Soc.*, *138*(665), 919–931, doi:10.1002/qj.962.

Roundy, P. E. (2012b), Observed structure of convectively coupled waves as a function of equivalent depth: Kelvin waves and the Madden-Julian oscillation, *J. Atmos. Sci.*, *69*(7), 2097–2106, doi:10.1175/JAS-D-12-03.1.

Roundy, P. E. (2012c), The spectrum of convectively coupled Kelvin waves and the Madden-Julian oscillation in regions of low-level easterly and westerly background flow, *J. Atmos. Sci.*, *69*(7), 2107–2111, doi:10.1175/JAS-D-12-060.1.

Schwartz, M. J., D. E. Waliser, B. Tian, D. L. Wu, J. H. Jiang, and W. G. Read (2008), Characterization of MJO-related upper tropospheric hydrological processes using MLS, *Geophys. Res. Lett.*, *35*(8), L08,812, doi:10.1029/2008GL033675.

Seidel, D. J., R. J. Ross, J. K. Angell, and G. C. Reid (2001), Climatological characteristics of the tropical tropopause as revealed by radiosondes, *J. Geophys. Res.*, *106*(D8), 7857–7878, doi:10.1029/2000JD900837.

Suzuki, J., and M. Shiotani (2008), Space-time variability of equatorial Kelvin waves and intraseasonal oscillations around the tropical tropopause, *J. Geophys. Res.*, *113* (D16), 110, doi:10.1029/2007JD009456.

Tian, B., C. O. Ao, D. E. Waliser, E. J. Fetzer, A. J. Mannucci, and J. Teixeira (2012), Intraseasonal temperature variability in the upper troposphere and lower stratosphere from the GPS radio occultation measurements, *J. Geophys. Res.*, *117*(D15), 1–19, doi:10.1029/2012JD017715.

Virts, K. S., and J. M. Wallace (2010), Annual, interannual, and intraseasonal variability of tropical tropopause transition layer cirrus, *J. Atmos. Sci.*, *67* (10), 3097–3112, doi:10.1175/2010JAS3413.1.

Wheeler, M. C., and H. H. Hendon (2004), An all-season real-time multivariate MJO index: Development of an index for monitoring and prediction, *Mon. Weather Rev.*, *132*(8), 1917–1932, doi:10.1175/1520-0493(2004)132<1917:AARMMI>2.0.CO;2.

Wilks, D. S. (2011), *Statistical Methods in the Atmospheric Sciences*, vol. 100, Academic Press, Amsterdam, Netherlands.

Zhang, C. (1996), Atmospheric intraseasonal variability at the surface in the tropical western pacific ocean, *J. Atmos. Sci.*, *53*(5), 739–758, doi:10.1175/1520-0469(1996)053<0739:AIVATS>2.0.CO;2.

Zhang, C. (2005), Madden-Julian oscillation, *Rev. Geophys.*, *43*(2), 1–36, doi:10.1029/2004RG000158.

Zhang, C., and M. J. McPhaden (2000), Intraseasonal surface cooling in the equatorial western pacific, *J. Climate*, *13*(13), 2261–2276, doi:10.1175/1520-0442(2000)013<2261:ISCITE>2.0.CO;2.